Optics & Laser Technology 161 (2023) 109228

Contents lists available at ScienceDirect

Optics and Laser Technology

journal homepage: www.elsevier.com/locate/optlastec

Full length article

Breakthrough light harvesting in time-domain diffuse optics with 100 mm^2 silicon photomultiplier

Laura Di Sieno [a,*], Elisabetta Avanzi [a], Anurag Behera [a], Pietro Levoni [a], Fabio Acerbi [b], Alberto Gola [b], Lorenzo Spinelli [c], Alessandro Torricelli [a,c], Alberto Dalla Mora [a]

[a] Politecnico di Milano, Dipartimento di Fisica, Piazza Leonardo da Vinci, 32, Milano 20133, Italy
[b] Fondazione Bruno Kessler (FBK), Via Sommarive, 18, Trento 38123, Italy
[c] Consiglio Nazionale delle Ricerche, Istituto di Fotonica e Nanotecnologie, Piazza Leonardo da Vinci, 32, Milano 20133, Italy

ARTICLE INFO

Keywords:
Photon counting
Solid state detectors
Photon migration
Turbid media
Spectroscopy
Time-resolved

ABSTRACT

Time-Domain Diffuse Optics (TDDO) technologies are rapidly evolving towards compact and cheap devices, thus progressively reducing the gap with continuous-wave equivalent technologies while providing the additional advantages of higher information content and better depth penetration and selectivity. One of the key limitations for TDDO is the active area of microelectronic time-resolved single-photon detectors as it is not possible to efficiently focus Lambertian light exiting from highly scattering samples into small areas. Therefore, signal-to-noise ratio bottlenecks can be surpassed only by targeting a breakthrough in this direction. In this work we present the validation in laboratory settings of the largest detector (100 mm^2 active area with 92% cells fill-factor) ever reported to our knowledge in TDDO applications. To objectively validate this device, we made use of established performance assessment protocols in the field of diffuse optics, which also define standard conditions enabling realistic benchmarking of novel devices. The detector demonstrated the largest light harvesting capability ever reported, capability to measure homogeneous optical properties in line with state-of-the-art devices, and superior depth penetration inside heterogeneous media (in reflectance geometry) with respect to all the previously reported technologies (i.e., >4 cm). The active area breakthrough permits to envisage the first TDDO measurements on different fruits in transmittance geometry, thus increasing the penetration depth with respect to the traditional reflectance approach and making it easier for a future evolution towards real time quality check of fruits on the conveyor belt.

1. Introduction

Diffuse optics is an established technique exploiting light propagation inside highly scattering media like biological tissues, fruits, and vegetables to non-invasively and non-destructively assess their chemical composition and microstructure [1]. Light is both shone and collected at the surface of the sample under investigation either in reflectance (i.e., source and detector are placed on the same side of the sample at a given distance) or transmittance (i.e., source and detector are placed on opposite sides of the sample) geometry [2], obtaining information about deep (few cm) structures. The reflectance geometry is usually adopted when the thickness of the sample is larger than 6–8 cm [3] (depending on optical properties) as this prevents the transmittance approach due to the strong attenuation of light produced by photon diffusion and absorption. However, in reflectance geometry with commonly adopted source-detector separations (i.e., 1–4 cm), the sensitivity typically peaks at depths <2.5 cm [4]. Therefore, the deeper parts of samples thicker than 5 cm could in principle be better probed in a transmittance approach.

Among different possible implementations, Time-Domain Diffuse Optics (TDDO) is recognized as the one with more informative content associated to each source-detector pair, since absorption and scattering information are intrinsically disentangled and the investigated depth is naturally encoded in the photon arrival time [3]. However, at the same time, it suffers from poor Signal-to-Noise Ratio (SNR) because light is collected at single-photon level [5], requiring the reconstruction of the histogram of photons' arrival time through the Time-Correlated Single-Photon Counting (TCSPC) technique [6]. In particular, the adoption of detectors with large active area and high numerical aperture is fundamental because the Lambertian emission of light from the sample

* Corresponding author.
E-mail address: laura.disieno@polimi.it (L. Di Sieno).

https://doi.org/10.1016/j.optlastec.2023.109228
Received 10 November 2022; Received in revised form 28 December 2022; Accepted 24 January 2023
Available online 7 February 2023

prevents the possibility to focus it onto small-area detectors. Due to this limitation, for instance, TDDO measurements on medium sized fruits and vegetables (e.g., apples, pears, etc.) in order to assess their quality/ripening have always been performed with a reflectance geometry [7], while transmittance measurements were possible with continuous-wave diffuse optics thanks to the availability of powerful light sources (e.g., halogen lamps) and large area detectors (e.g., charge-coupled device cameras) [8–11].

Traditionally, in TDDO applications, photomultiplier tubes coupled to the sample through large-core (e.g., 1 mm) optical fibers or fiber bundles are the primary choice for light detection, but microelectronic detectors like Single-Photon Avalanche Diodes (SPADs) started gaining attention because of their robustness, compact size, and scalability [3], which also allowed them to be placed directly in contact with the sample under investigation, avoiding the use of optical fibers and maximizing the numerical aperture of the detection chain [3,12]. Since the active area diameter of SPADs is limited to few hundred micrometers, Silicon PhotoMultipliers (SiPMs) have been gradually introduced in TDDO, thus gaining orders of magnitude of light harvesting efficiency thanks to their $\geq$1 mm^2 active area [13].

In 2020, Di Sieno *et al.* [14] successfully validated a commercially available 3 × 3 mm^2 active area SiPM, with 82% cell fill-factor (i.e., 7.38 mm^2 effective active area), coupled with a custom-made high-performance front-end circuit, thus allowing to strongly increase the SNR by running beyond the single-photon statistics. Similarly, in 2021, Di Sieno *et al.* [15] demonstrated the performances of a custom-made 8.6 mm^2 effective active area CMOS digital SiPM with also time-gated capability to avoid the collection of scarcely diffused early photons, avoiding the saturation of the detector at high photon fluxes. Finally, in 2022, Behera *et al.* [16] demonstrated the possibility to operate a 6 × 6 mm^2 SiPM, with 89.2% cell fill-factor (i.e., 32.1 mm^2 effective active area), specifically developed for TDDO. To date, this represents the largest active area detector ever demonstrated in the field. In particular, it allowed the researchers to probe different parts of the human body with unmatched source-detector separations up to 16 cm.

It is worth noting that each step in the increase of the maximum feasible SiPM area has been obtained overcoming specific technological challenges in order to get performances in line with TDDO needs, requiring in particular to limit concurrent detrimental effects in the fabrication process yield, dark count rate, and detector timing response shape.

This evolution not only increased the collection efficiency of diffused photons by orders of magnitude with respect to traditional approaches, but has now led to the exploration of unprecedented concepts like the possibility to monitor deep organs in the human chest (e.g., lungs [17]). However, a complete change of paradigm like the possibility to switch from reflectance to transmittance measurements in a given application has yet to be demonstrated.

In this work, we present the validation of a 10 × 10 mm^2 active area SiPM module (in the following 100 mm^2 module) specifically developed for TDDO applications, with 92% cell fill-factor (i.e., 92.1 mm^2 effective active area), which represents the largest device ever reported in the field [18]. Tests are performed using internationally agreed rigorous protocols for performance assessment of diffuse optical systems. Thanks to its unique photon collection efficiency of diffused light, here we demonstrate for the first time the possibility to probe different fruits in transmittance geometry. This arrangement would represent a breakthrough in the field in two ways. First, it allows for better probing of deeper regions within the fruit. Second, it could allow an easier and more reliable application in the production chain as transmittance measurements are usually more insensitive to artefacts like direct light channeling from the source to the detector point due to unwanted propagation of light, easily occurring in the thin air gap between the probe and the fruit surface [19,20], thus also simplifying the adoption of non-contact detection schemes.

2. Detector description and performance validation

In this section, the 100 mm^2 module as well as its characterization on phantom are described. To assess the performances of the proposed detector, three internationally shared protocols for diffuse optics instruments are applied. More in detail, Basic Instrumental Performances (BIP) protocol deals with the hardware performance of the instrument (without considering any diffusive media), MEDPHOT protocol assess the capability of the system to recover optical properties of homogeneous media, while nEUROPt protocol evaluates the sensitivity to optical inhomogeneity buried in depth [16].

2.1. Detector description

The detector module dimensions are 60 × 73 × 58 mm^3, as reported in Fig. 1(a). The front part is composed of metal heatsink, while the backside is a 3D printed plastic manufactured enclosure. The module is based on a large area SiPM with a nominal dimension of 10 × 10 mm^2, based on a modified near infra-red, high density of cells technology, with 50 μm cell pitch, designed and fabricated by FBK (Trento, Italy) [18]. Despite being a single silicon chip, the SiPM is composed of 6 sub-SiPMs (each one having dimensions of 4.88 × 3.25 mm^2), externally connected in 2 groups, then combined in the front-end. The SiPM is packaged into a TO822 case, including a Peltier Thermoelectric Cooler (TEC) and temperature controller, which is based on a linear stage with a compact heat sink. The SiPM is cooled to −36 ± 1.5 °C, to provide a primary dark count rate of about 900 kcps (i.e., kilocounts per second) at 5 V of excess bias (i.e., 34.1 V bias). In these conditions, the direct crosstalk probability is nearly 20%, while the afterpulsing and the delayed crosstalk are almost negligible (~2%). To cool down both the front heatsink and the TEC, a fan is placed on the back of the module. A ±5 V and +10 V voltage supply are used to power the front-end, the temperature controller, and the auxiliary electronics. Ref. [18] contains more details about the electronic design and the characterization of the module.

2.2. Experimental setup

The experimental setup adopted is shown in Fig. 1(b). A laser source with a repetition rate of 40 MHz was employed to generate laser pulses. For the BIP protocol, the source was a supercontinuum laser (SuperK Extreme, NKT Photonics, Denmark) combined with a home-made wavelength-selection stage based on a rotating prism, operating over a wide range of wavelengths (from 600 to 1100 nm), thus resulting in an average output power in the range of few hundreds of μW/nm. For the MEDPHOT and the nEUROPt protocols, a diode laser with emission wavelength centered at 670 nm (LDH-P-670, Picoquant GmbH, Germany) and with output power capable of providing up to 50 mW was used. Then, a circular variable neutral density filter installed on a fiber-to-fiber u-branch was employed to control the output laser light intensity, setting the desired photon counting rate. The attenuated light was then delivered into the sample before being recorded by the detector. The histograms of the Distribution of Time-Of-Flight (DTOF) were generated using a PC-hosted TCSPC board (SPC-130, Becker & Hickl GmbH, Germany). The start and stop signals were provided by the SiPM module output and the laser synchronization signal, respectively. Commercially available power supply units were used to bias the module (i.e., the detector, the front-end amplifier, and the TEC).

2.3. Performance assessment

To assess the performance of the detector (without any diffusive medium), we used some tests of the BIP protocol, namely responsivity of the detection chain and Instrument Response Function (IRF).

Responsivity represents the overall diffused light collection capability of the detection chain, and it is impacted not only by the quantum

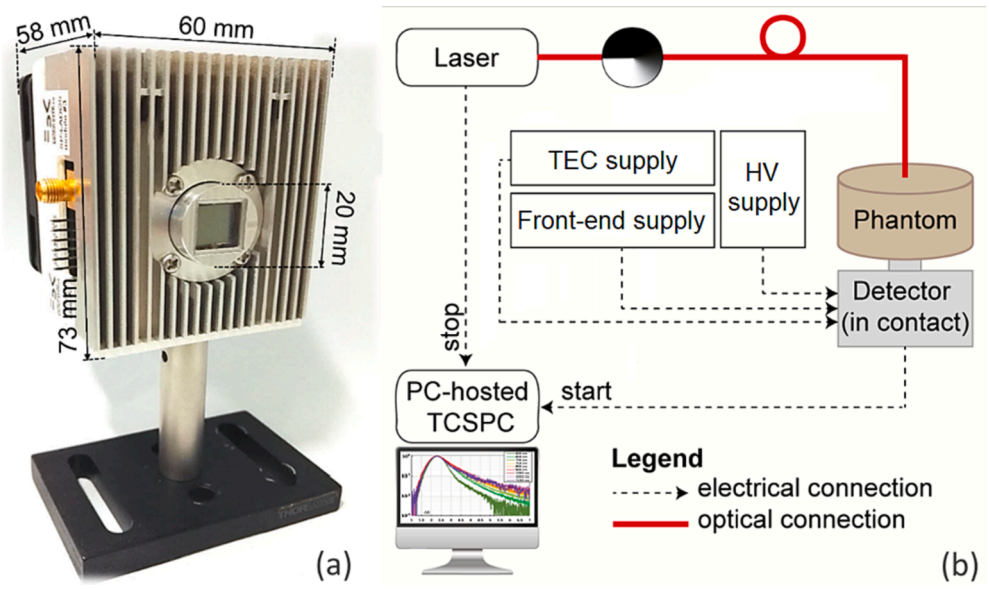

Fig. 1. Picture of the 100 mm^2 module (a) and schematics of the setup used for the measurements (b).

efficiency but also by the active area, fill factor, and numerical aperture of the detector. A solid phantom of known photon transmittance factor was used to convert the injected power to wavelength-dependent photon radiance. As dictated by the BIP protocol, 20 acquisitions of 1 s were taken for each wavelength covering a spectrum from 600 to 1100 nm in steps of 50 nm. Fig. 2 shows the spectral responsivity of the 100 mm^2 module, compared to other large area detectors such as 36 mm^2 [16], 9 mm^2 [14] and 1.7 mm^2 [13] SiPM module (all in fiber-less configuration). As clearly visible, the 100 mm^2 module has a responsivity that exceeds 10^{-4} m^{2}sr (for wavelengths shorter than 750 nm) representing, to the best of our knowledge, the highest value ever reached by a diffuse optics system. The improvement is on average about a factor of 5, 10 and nearly 100 if compared to cutting-edge (36 mm^2 [16] and 9 mm^2 [14] SiPM) and state-of-the-art detectors (1.7 mm^2 [13] SiPM). The responsivity of the 100 mm^2 at 670 and 830 nm (i.e., the wavelengths used for the following validation of fruits) has been computed to be 1.41 10^{-4} and 4.28 10^{-5} m^{2}sr for 670 and 830 nm, respectively.

Concerning the IRF shape, Fig. 3 reports the curves obtained in the spectral range from 600 to 1100 nm with an integration time of 1 s. The reported curves have been background subtracted and their temporal position and amplitude have been normalized and aligned for visualization purposes. The dynamic range of the IRF is about 2 decades and it is affected by the diffusion tail of the SiPM which is more limiting for longer wavelength, as clearly visible from Fig. 3. The temporal resolution (expressed as Full-Width at Half Maximum, FWHM) ranges from 734.9 ps at 600 nm to 891.5 ps at 1100 nm.

Thanks to the very large responsivity, the proposed module is considered suitable for diffuse optical measurements despite the timing resolution in the order of hundreds of ps. This is especially true when using transmittance geometry in thick samples where the enlargement of the DTOF is considerable.

The MEDPHOT protocol evaluates the ability of a system to linearly follow changes in optical properties over a large range. It also evaluates the accuracy and precision of the retrieved values. A set of 32 standard homogeneous solid phantoms were used. They span a wide range of absorption (8 reference values from 0 to 0.49 cm^{-1} at steps of about 0.07 cm^{-1} measured at 670 nm) and reduced scattering (4 reference values from 7 to 20 cm^{-1} at steps of about 4 cm^{-1} at 670 nm)

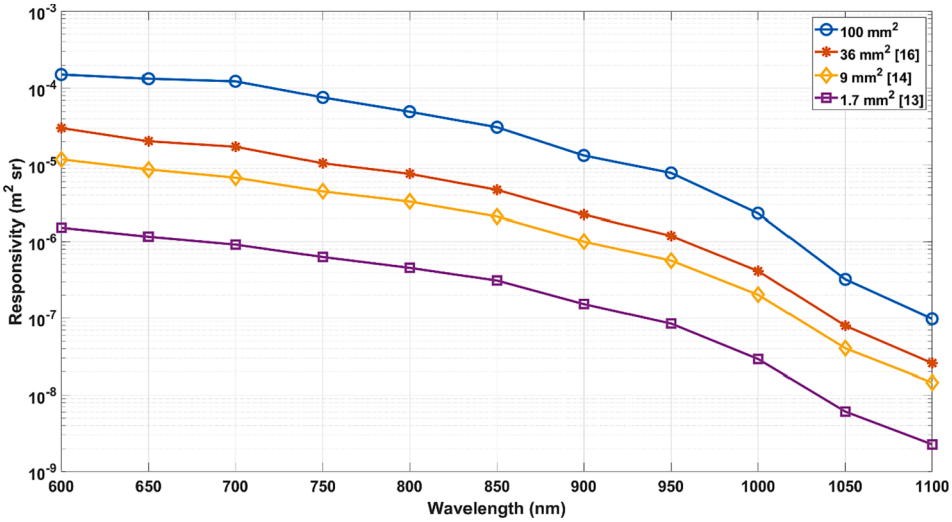

Fig. 2. Spectral responsivity of the 100 mm^2 module compared to other SiPM detectors validated in TDDO applications (36 mm^2 [16], 9 mm^2 [14] and 1.7 mm^2 [13] SiPM module in fiber-less configuration).

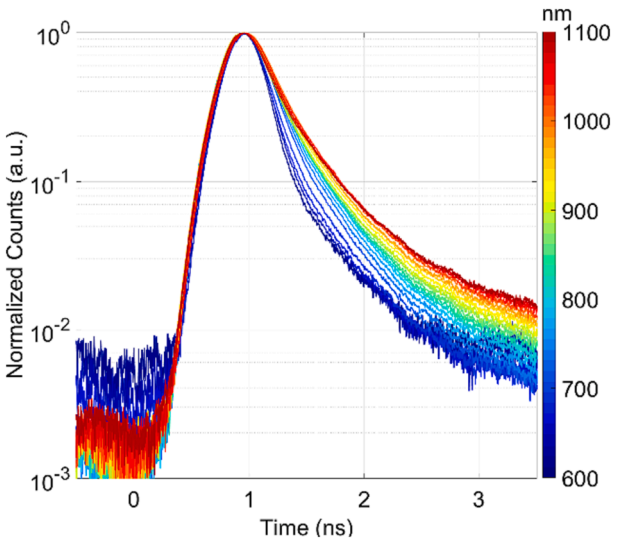

Fig. 3. IRF recorded at different wavelengths (colors), after normalization in time and amplitude.

coefficients. The complete references values of the phantoms are reported in legend of Fig. 4. The measurements were performed in transmittance geometry, with an average phantom thickness of about 4.5 cm. The setup shown in Fig. 1(b) was used for the measurements. For each phantom, 60 acquisitions of 1 s each were taken. To improve the overall SNR, all curves were summed up. To recover the optical properties a fitting procedure (as described in [21]) based on analytical solution of radiative transport equation under the diffusion approximation in transmittance geometry for a homogeneous slab using partial current boundary conditions [22] was employed. The theoretical homogeneous curve generated by the model was convolved with the experimentally obtained IRF. Using a Levenberg-Marquardt minimization procedure, the model-based curves were fitted to the experimentally obtained ones to retrieve μ_a and μ_s'. The retrieved optical properties were used to evaluate the ability of the system in following changes in μ_a and μ_s' (linearity test, Fig. 4(a) and Fig. 4(d), respectively), as well as the dependence of retrieving μ_a on μ_s' and vice versa (scattering-to-absorption -Fig. 4(b)- and absorption-to-scattering coupling -Fig. 4(c)-, respectively). The linearity in the retrieval of both μ_a and μ_s' is good with only slight deviation from the linear behavior. Further, the coupling between the nominal μ_s' and the measured μ_a is almost negligible (mostly for phantom with $\mu_a < 0.34$ cm^{-1}), while the coupling between the nominal μ_a and the μ_s' is stronger.

The nEUROPt protocol evaluates the ability of the system in detecting local absorption changes within a homogeneous background. A totally absorbing inclusion of 100 mm^3 volume, corresponding to an absorption change ($\Delta\mu_a$) of 0.16 cm^{-1} over a volume of 1 cm^3 [23], was used as an absorption perturbation within a homogeneous liquid phantom. This liquid phantom was composed of calibrated quantities of Intralipid, water and ink whose quantities were adjusted to have the desired optical properties ($\mu_a = 0.1$ cm^{-1} and $\mu_s' = 10$ cm^{-1}) at 670 nm [24]. The inclusion was translated in depth by a motorized stage, with the distance from the liquid surface to the center of the inclusion measured as Z (i.e., the depth of the perturbation). The reflectance curves were acquired for different inclusion depths ranging from 0.25 cm to 5 cm in steps of 0.2 cm, with Z = 6 cm corresponding to the homogeneous condition (i.e., where the effect of the perturbation is negligible). For each position, 10 acquisitions of 1 s each were acquired. This procedure was repeated for different source-detector separations (ρ): i) a commonly used standard condition ($\rho = 3$ cm); ii) uncommon large distances enabled by the high detector sensitivity ($\rho = 6$ to 12 cm at steps of 1 cm). For each source-detector separation, contrast and Contrast-to-Noise Ratio (CNR) were calculated. Contrast is computed as the normalized variation in the number of counts due the introduction of the absorption inhomogeneity and CNR indicates how this change in the number of counts compares with the overall fluctuations of the system. Contrast and CNR are computed as reported in Eqs. (1) and (2):

$$C = \frac{N_0 - N}{N_0} \tag{1}$$

$$CNR = \frac{N_0 - N}{\sigma(N_0)} \tag{2}$$

where N and N_0 are the inhomogeneous and homogeneous counts (i.e., with and without perturbation) respectively and $\sigma(N_0)$ is the standard deviation of the homogeneous counts among the different repetitions. Contrast and CNR can be computed using selected portions of the DTOF (i.e., time gates) to enhance the information at different depths. Their temporal position is referred to the IRF peak. In all cases, the background noise was subtracted before computing the figure of merits.

Fig. 5 and Fig. 6 report the contrast and the CNR obtained for different ρ (colors and markers) and for the different time-gates (panels), whose width was set to 1 ns. Fig. 5 indicates clearly that the use of later time-gates permits one to probe deeper regions. Moreover, the use of large source-detector distances improves the sensitivity in depth, thus permitting to detect perturbations up to 40 mm. Indeed, setting 1% as a threshold value for the minimum contrast (considered as the minimum change distinguishable in living tissues), using a source-detector separation of 10 cm in a time-gate delayed 6–7 ns from the IRF peak the maximum penetration depth (4.05 cm) can be achieved, slightly overcoming the best results obtained with more complex techniques (e.g., time gating [15]). For this value, as visible from Fig. 6 the CNR is larger than 1 (value which ensures that the effect given by the perturbation is distinguishable being larger than fluctuations in the number of counts). Moreover, Fig. 5 and Fig. 6 also clearly show that the use of $\rho > 10$ cm does not improve the depth sensitivity, since a lower signal is detected, thus demoting the CNR (points with CNR < 1 are not displayed in Fig. 5).

3. Application to non-invasive fruit quality assessment

3.1. Simulations

Prior to implementing the setup and assessing the optical properties of any fruit, we proved the feasibility of transmittance TDDO measurements by performing simulations.

Firstly, we employed an in-house built software to simulate time resolved transmittance curves in diffusion equation approximation [25] for a homogeneous sample, adopting a cubic geometry. The refractive index of the sample was set to 1.4, a typical value for fruits [26]. The injection area was considered point like, while the detection area was set to 100 mm^2. We assessed various combinations of sample parameters typical of fruits, namely μ_a (set to 0.1, 0.2, 0.3 and 0.4 cm^{-1}), μ_s' (set to 10, 15, 20 and 25 cm^{-1}), and size (cube's side of 6, 8, 10 and 12 cm).

Afterwards, we fed each simulated curve to a MATLAB script which convolves it with a test IRF (properly freed from background and normalized to unitary area) and then rescales the convolution based on the detector responsivity, so to simulate a measured transmittance curve. The detector responsivity was set to 1.41 10^{-4} and 4.28 10^{-5} m^{2}sr for 670 and 830 nm respectively, according to data obtained from the detector characterization.

The results are expressed in terms of the detected number of counts N_{det}, given by

$$N_{det} = t_{acq}\frac{s_{det}^L(\lambda)}{\pi}T_{tot}\cdot N_{in} \tag{3}$$

where t_{acq} is the acquisition time, which we arbitrarily set to 1 s, $s_{det}^L(\lambda)$ is the detector responsivity (which changes with the injection wavelength,

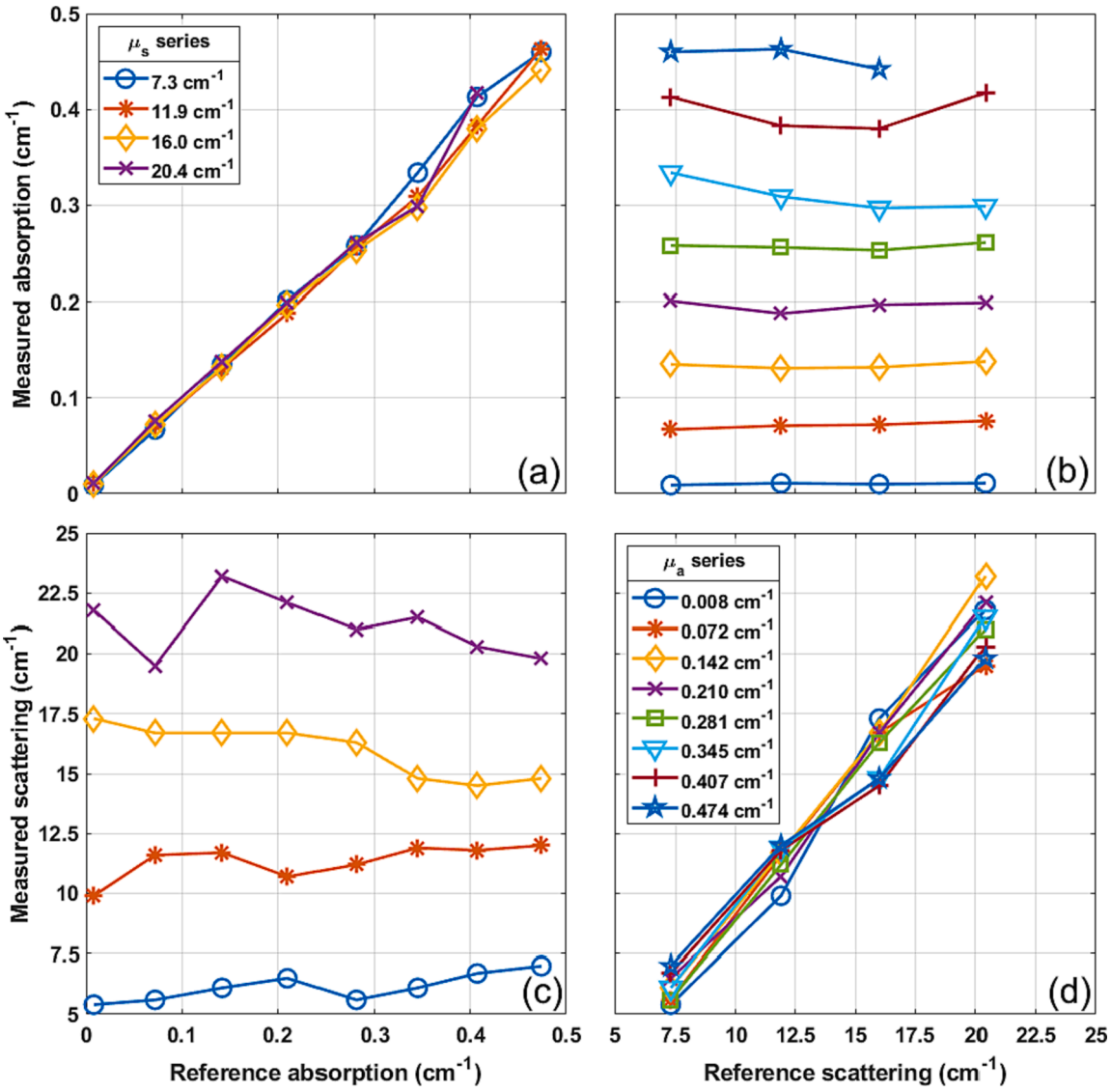

Fig. 4. MEDPHOT protocol results: measured absorption and scattering coefficients as a function of the references ones. Absorption linearity (a), scattering-to-absorption coupling (b), absorption-to-scattering coupling (c), and scattering linearity (d).

λ), T_{tot} is the total diffuse transmittance (i.e., the integral over time of the transmittance curve [21]), and N_{in} is the injected count rate, given by

$$N_{in} = \frac{P_{in}\lambda}{hc} \tag{4}$$

where P_{in} is the injected power (set to 10 mW, in line with the maximum experimental power conveyed on the samples), h is Planck's constant and c is the speed of light in vacuum.

The results of the simulations at 670 nm and at 830 nm are shown in Table 1. Counts lower than 10^3 have not been considered since this value experimentally represents the threshold value identifying feasible measurements. On the other hand, for values larger than 1000 photons, the range of the number of counts has been reported to give an idea of the signal level available. For larger size of the sample (10 and 12 cm), only a few cases (with relaxed optical properties, i.e., low absorption and reduced scattering) are feasible.

Overall, the results of the simulations suggest that, for certain combinations of absorption coefficient, reduced scattering coefficient and sample size, TDDO measurements in transmittance geometry are feasible, especially at 830 nm since in fruit the absorption coefficient is much lower than at 670 nm [26]. Therefore, we decided to proceed by implementing the setup and assessing the optical properties of a set of fruits.

3.2. Experimental validation

The experimental setup for the non-invasive fruit quality assessment is similar to the one described in the previous section. For this test, a 670 nm and an 830 nm laser head (LDH-P-C-670M and LDH-P-C-830M, Picoquant GmbH, Germany) were used alternately, such that each sample (i.e., the fruit of interest) was inspected at both wavelengths. Indeed, the two wavelengths are more sensitive to different chromophores: 670 nm to the chlorophyll, while 830 nm to water. The maximum power delivered on the fruit is about 24 mW and 11 mW at 670 and 830 nm, respectively. A set of fruits of different sizes, types of core and peelings was considered. We analyzed in transmittance geometry: plum (thickness of 6.3 cm), peach (thickness of 6.8 cm), orange (thickness of 7.5 cm), apple (thickness of 7.7 cm), papaya (thickness of 8.9 cm) and mango (thickness of 9.6 cm).

To reject the fluorescence signal generated only when the laser operating at 670 nm was employed, a narrow (10 nm FWHM) band pass filter (FB670-10, Thorlabs Inc., United States) was placed in contact between the detector and the fruit. For each fruit, at each wavelength 10

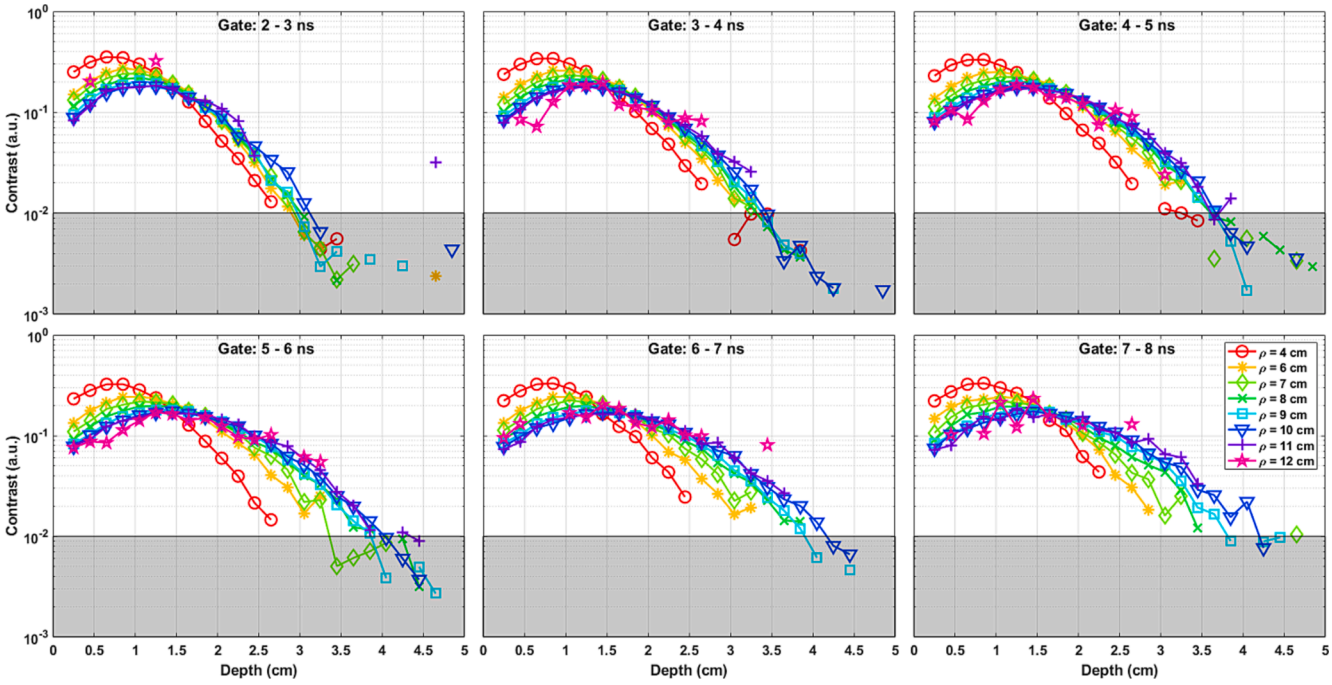

Fig. 5. nEUROPt protocol results: contrast produced by the absorption perturbation as a function of its depth for different source-detector separations (colors and markers) and different time-gates used for analysis (panels).

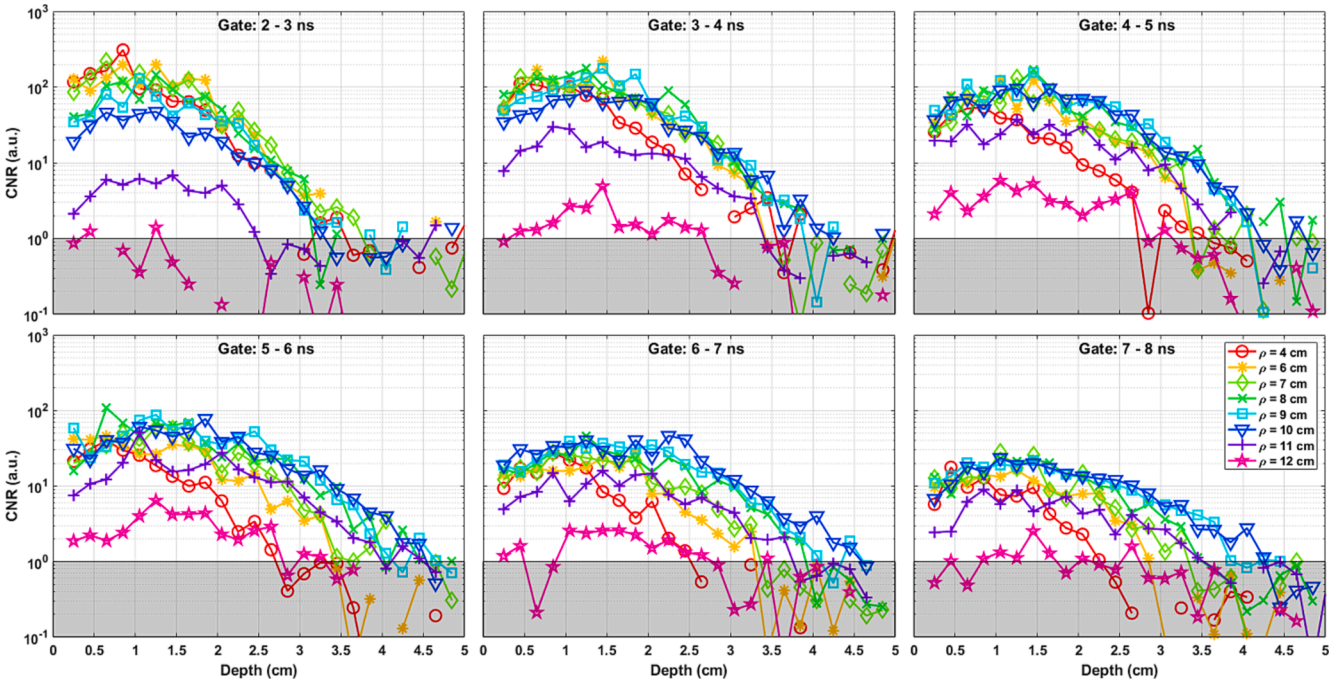

Fig. 6. nEUROPt protocol results: contrast-to-noise ratio produced by the absorption perturbation as a function of its depth for different source-detector separations (colors and markers) and different time-gates used for analysis (panels).

acquisitions of 1 s each were performed and summed up to increase the overall SNR. Before and after each fruit measurement at each wavelength, the IRF was acquired to fit the recorded DTOFs and extract the optical properties. To fit the data the analytical model of photon transport in a diffusive parallelepiped under the diffusion approximation was used [25].

Fig. 7 reports the measured μ_a and μ_s' of the fruits, plotted against the two wavelengths used. It is evident that the large responsivity of the 100 mm^2 module allows us to retrieve optical properties of samples whose thickness reached the considerable value of 9.6 cm.

For the absorption coefficients (Fig. 7(a)), it is possible to see that the retrieved values at 830 nm were greater than those obtained at 670 nm for all the measured fruits (except plum, which is an exception due to the inner colored pulp associated with a high presence of anthocianines [27]). Such low values are compatible with the structure and the stage of maturation of the measured fruits, in particular the orange whose μ_a passed from ~1 10^{-6} cm^{-1} at 670 nm to 0.0078 cm^{-1} at 830 nm. Indeed, it is mainly composed by water with low percentage of chlorophyll due

Table 1
Table summarizing the results obtained from simulations. Values are expressed in counts per second.

			670 nm				830 nm			
Size ↓	**μ_a ↓**	**μ_s' →**	**10 cm^{-1}**	**15 cm^{-1}**	**20 cm^{-1}**	**25 cm^{-1}**	**10 cm^{-1}**	**15 cm^{-1}**	**20 cm^{-1}**	**25 cm^{-1}**
6 cm	**0.1 cm^{-1}**		$>10^6$	$>10^6$	$>10^6$	$>10^6$	$>10^6$	$>10^6$	$>10^6$	$>10^6$
	0.2 cm^{-1}		$>10^6$	$>10^6$	10^5-10^6	10^4-10^5	$>10^6$	10^5-10^6	10^4-10^5	10^3-10^4
	0.3 cm^{-1}		$>10^6$	10^4-10^5	10^3-10^4	no	10^5-10^6	10^4-10^5	no	no
	0.4 cm^{-1}		10^5-10^6	10^3-10^4	no	no	10^4-10^5	no	no	no
8 cm	**0.1 cm^{-1}**		$>10^6$	$>10^6$	10^5-10^6	10^4-10^5	$>10^6$	10^5-10^6	10^4-10^5	10^3-10^4
	0.2 cm^{-1}		10^5-10^6	10^3-10^4	no	no	10^4-10^5	10^3-10^4	no	no
	0.3 cm^{-1}		10^3-10^4	no	no	no	10^3-10^4	no	no	no
	0.4 cm^{-1}		no	no	no	no	no	no	no	no
10 cm	**0.1 cm^{-1}**		$>10^6$	10^4-10^5	10^3-10^4	no	10^5-10^6	10^4-10^5	no	no
	0.2 cm^{-1}		10^3-10^4	no	no	no	no	no	no	no
	0.3 cm^{-1}		<100	no	no	no	no	no	no	no
	0.4 cm^{-1}		no	no	no	no	no	no	no	no
12 cm	**0.1 cm^{-1}**		10^4-10^5	no	no	no	10^4-10^5	no	no	no
	0.2 cm^{-1}		no	no	no	no	no	no	no	no
	0.3 cm^{-1}		no	no	no	no	no	no	no	no
	0.4 cm^{-1}		no	no	no	no	no	no	no	no

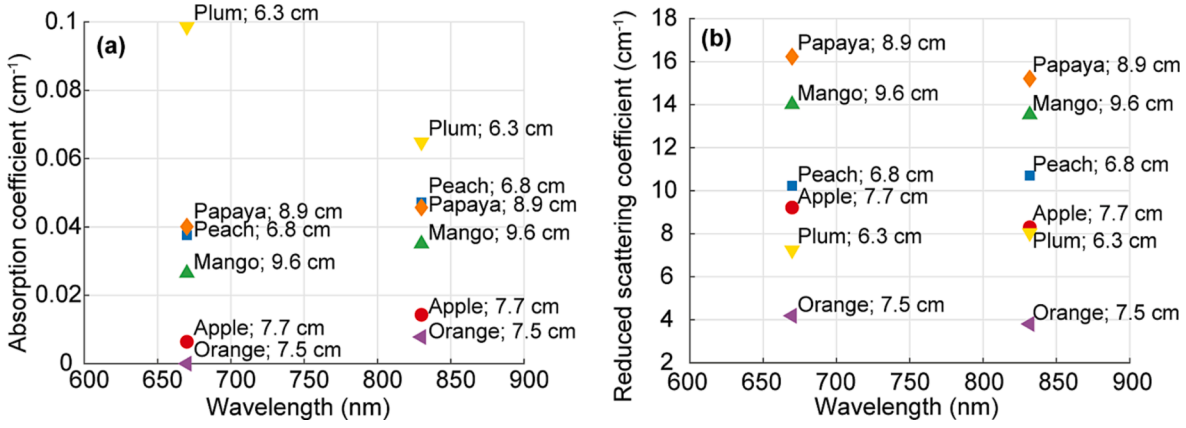

Fig. 7. Measured absorption (a) and reduced scattering (b) coefficient for various fruits, at 670 and 830 nm. Each point is labeled with the name and the thickness of the measured fruit.

to its high ripeness.

For the reduced scattering coefficients (Fig. 7(b)), the retrieved values were generally greater when the fruit was probed at 670 nm rather than at 830 nm (increase of 7.81% is obtained on average for apple, mango, orange, and papaya), as expected from Mie theory [28]. Peach and plum, instead, showed a reduction of μ_s' of 4.48% and 9.95%, respectively. It is worth noting that the μ_s' of the orange, which had a watery pulp, was almost four times lower than that of the papaya, characterized by a dense pulp (orange: $\mu_s' = 4.19\ cm^{-1}$ at 670 nm and $\mu_s' = 3.81\ cm^{-1}$ at 830 nm, papaya: $\mu_s' = 16.23\ cm^{-1}$ at 670 nm and $\mu_s' = 15.21\ cm^{-1}$ at 830 nm).

To conclude, the 100 mm^2 SiPM module allows one to measure all samples in transmittance geometry, even for fruits with large dimensions (e.g., mango with thickness of 9.6 cm). The recovered optical properties are reasonable, considering the fruits and their maturation stage, even though it is not among the scope of this paper the precise retrieval of the optical properties.

4. Conclusions and future perspectives

In this manuscript, we report the performance of the 100 mm^2 SiPM module which is, to the best of our knowledge, the largest time-resolved single-photon detector ever proposed for diffuse optics applications. From BIP protocol, we verified the largest responsivity (i.e., diffuse light harvesting capability) ever reported with an improvement of about one million with respect to state-of-the-art TDDO system for fruit assessment currently in use [29]. Such a large active area (92.1 mm^2) results in a large IRF (temporal resolution < 900 ps) with a dynamic range of about 2 decades that, however, is still suitable for TDDO in transmittance geometry on thick samples. In this geometry, indeed, the 100 mm^2 module is capable of linearly retrieving variations in absorption and reduced scattering coefficient with limited coupling between optical coefficients (as verified by MEDPHOT protocol).

Moreover, we tested in reflectance geometry the capability of the 100 mm^2 module to detect an inhomogeneity buried in depth. In this context we achieved record performances: indeed, we reached the largest penetration depth (4.05 cm) ever achieved, overcoming the 3.75 cm set by a more complicated techniques (i.e., large area time-gated SiPM [15]). These findings can open the way to other applications in different fields (e.g., the assessment of composition and oxygenation of the lung).

Thanks to the encouraging results obtained with the protocols, we adopted the 100 mm^2 module for proof-of-principle non-invasive measurements of fruits in transmittance geometry. After studying by simulations the feasibility of the proposed approach, we measured several fruits with a maximum thickness of about 9.6 cm, opening the way to a new way to assess fruit ripeness and quality. Indeed, the use of TDDO technique coupled to large light harvesting capability detector, will allow to work in transmittance geometry (thus probing the whole area of the fruit reducing issues such as direct light) with high throughput and to separate the assessment of texture of the fruit from its ripening. Indeed, the possibility to disentangle scattering (related to the fruit

texture) from absorption (connected to the presence of chromophores such as chlorophyll, water and carotenoids) allows one to retrieve separately the information on the texture from that on the fruit maturity. Moreover, TDDO measurements in transmittance geometry permit to probe the center of the fruit thus identifying possible defects (e.g., brown heart and/or water core). All those advantages go in the direction of better exploitation of fruits, thus sustaining the circular economy. Thanks to the large active area, also a non-contact and/or fast scanning system can be envisaged as future perspectives.

However, this work represents a first step in this direction: a more accurate modelling of the light diffusion in heterogeneous fruits (e.g., presence of core and/or not homogeneous pulp) is needed to provide reasonable values of μ_a and μ_s' and to further test the device performances in this particular application. Indeed, in this manuscript, only average values obtained considering the fruit a homogeneous medium are reported with the only scope to demonstrate the possibility to measure fruits in transmittance geometry.

Data availability

The data that support the findings of this study are available from the corresponding author upon reasonable request.

Funding

This work was supported in part by the ATTRACT project "SPLADOS" funded by the EU under Grant Agreement 777222, and by the ESPERA project funded by Regione Lombardia under Grant Agreement 17 (Bando per il finanziamento di progetti di ricerca in campo agricolo e forestale - D.D.S. 4403/2018).

This study was carried out within the Agritech National Research Center and received funding from the European Union NextGenerationEU (PIANO NAZIONALE DI RIPRESA E RESILIENZA (PNRR) – MISSIONE 4 COMPONENTE 2, INVESTIMENTO 1.4 – D.D. 1032 17/06/2022, CN00000022). This manuscript reflects only the authors' views and opinions, neither the European Union nor the European Commission can be considered responsible for them.

CRediT authorship contribution statement

Laura Di Sieno: Conceptualization, Methodology, Formal analysis, Writing – original draft, Funding acquisition. **Elisabetta Avanzi:** Investigation, Formal analysis, Writing – original draft. **Anurag Behera:** Investigation, Formal analysis, Writing – original draft. **Pietro Levoni:** Investigation, Formal analysis, Writing – original draft. **Fabio Acerbi:** Conceptualization, Methodology, Writing – review & editing. **Alberto Gola:** Conceptualization, Methodology. **Lorenzo Spinelli:** Methodology, Formal analysis, Writing – review & editing. **Alessandro Torricelli:** Methodology, Formal analysis, Writing – review & editing. **Alberto Dalla Mora:** Conceptualization, Methodology, Writing – original draft.

Declaration of Competing Interest

The authors declare the following financial interests/personal relationships which may be considered as potential competing interests: Alberto Dalla Mora reports a relationship with pioNIRS srl that includes: board membership and equity or stocks. Alessandro Torricelli reports a relationship with pioNIRS srl that includes: board membership and equity or stocks.

Data availability

Data will be made available on request.

Acknowledgements

We thank Paolo Di Stefano, Lorenzo Fantauzzi, Fabio Saretto, and Matteo Scaietti for their support during the experimental validation.

References

[1] A. Yodh, B. Chance, Spectroscopy and imaging with diffusing light, Phys. Today 48 (1995) 34.
[2] T. Durduran, R. Choe, W.B. Baker, A.G. Yodh, Diffuse optics for tissue monitoring and tomography, Rep. Prog. Phys. 73 (2010), 076701.
[3] A. Pifferi, D. Contini, A. Dalla Mora, A. Farina, L. Spinelli, A. Torricelli, New frontiers in time-domain diffuse optics, a review, J. Biomed. Opt. 21 (2016), 091310.
[4] F. Martelli, T. Binzoni, A. Pifferi, L. Spinelli, A. Farina, A. Torricelli, There's plenty of light at the bottom: statistics of photon penetration depth in random media, Sci. Rep. 6 (2016) 27057.
[5] M.B. Applegate, R.E. Istfan, S. Spink, A. Tank, D. Roblyer, Recent advances in high speed diffuse optical imaging in biomedicine, APL Photonics 5 (2020) 040802.
[6] Desmond V. O'Connor, David Phillips, Time-correlated single photon counting, Academic Press, New York, 1984.
[7] A. Torricelli, D. Contini, A. Dalla, Mora, E. Martinenghi, D. Tamborini, F. Villa, A. Tosi, L. Spinelli, Recent advances in time-resolved NIR spectroscopy for nondestructive assessment of fruit quality, Chem. Engineer. Trans. 44 (2015) 43.
[8] B.M. Nicolaï, K. Beullens, E. Bobelyn, A. Peirs, W. Saeys, K.I. Theron, J. Lammertyn, Nondestructive measurement of fruit and vegetable quality by means of NIR spectroscopy: A review, Postharvest Biol. Tec. 46 (2007) 99.
[9] J. Wang, Z. Guo, C. Zou, S. Jiang, H.R. El-Seedi, X. Zou, General model of multi-quality detection for apple from different origins by Vis/NIR transmittance spectroscopy, J. Food Meas. Charact. 16 (2022) 2582.
[10] D. Han, T.u. Runlin, L.u. Chao, X. Liu, Z. Wen, Nondestructive detection of brown core in the Chinese pear 'Yali' by transmission visible–NIR spectroscopy, Food Control 17 (2006) 604.
[11] A.V. McGlone, P.J. Martinsen, C.J. Clark, R.B. Jordan, On-line detection of Brownheart in Braeburn apples using near infrared transmission measurements, Postharvest Biol. Tec. 37 (2005) 142.
[12] S. Saha, S. Burri, C. Bruschini, E. Charbon, F. Lesage, M. Sawan, Time domain NIRS optode based on null/small source-detector distance for wearable applications, in 2019 IEEE Custom Integrated Circuits Conference (CICC), 2019, IEEE Austin, TX.
[13] A. Dalla Mora, L. Di Sieno, A. Behera, P. Taroni, D. Contini, A. Torricelli, A. Pifferi, The SiPM revolution in time-domain diffuse optics, Nucl. Instrum. Meth. A 978 (2020), 164411.
[14] L. Di Sieno, A. Behera, S. Rohilla, E. Ferocino, D. Contini, A. Torricelli, B. Krämer, F. Koberling, A. Pifferi, A. Dalla Mora, Probe-hosted large area silicon photomultiplier and high-throughput timing electronics for enhanced performance time-domain functional near-infrared spectroscopy, Biomed. Opt. Express 11 (2020) 6389.
[15] L. Di Sieno, et al., Time-domain diffuse optics with 8.6 mm ^{2} fast-gated SiPM for extreme light harvesting, Opt. Lett. 46 (2021) 424.
[16] A. Behera, F. Acerbi, A. Gola, A. Dalla Mora, L. Di Sieno, Performance of a 6 × 6 mm^2 SiPM module for time-domain diffuse optics, IEEE J. Sel. Top. Quant. 28 (2021) 3802910.
[17] Antonio Pifferi, Massimo Miniati, Andrea Farina, Sanathana Konugolu Venkata Sekar, Pranav Lanka, Alberto Dalla Mora, Paola Taroni, Initial non-invasive in vivo sensing of the lung using time domain diffuse optics, Preprint arXiv:2205.08211v1, 2022.
[18] F. Acerbi, A. Behera, Alberto Dalla, Mora Laura, Di Sieno, Alberto Gola, Single-photon detection module based on large-area silicon photomultipliers for Time-domain diffuse optics, Instruments 5 (2021) 18.
[19] S. Del Bianco, F. Martelli, F. Cignini, G. Zaccanti, A. Pifferi, A. Torricelli, A. Bassi, P. Taroni, R. Cubeddu, Liquid phantom for investigating light propagation through layered diffusive media, Opt. Express 12 (2004) 2102.
[20] N.A. Carbone, D.I. Iriarte, A. Juan, Pomarico, Wide field continuous wave reflectance optical topography including a clear layer on top of the diffusive surface, J. Near. Infrared Spec. 25 (2017) 165.
[21] D. Contini, F. Martelli, G. Zaccanti, Photon migration through a turbid slab described by a model based on diffusion approximation. I. Theory, Appl. Optics 36 (1997) 4587.
[22] R.C. Haskell, L.O. Svaasand, T.-T. Tsay, T.-C. Feng, M.S. McAdams, B.J. Tromberg, Boundary conditions for the diffusion equation in radiative transfer, J. Opt. Soc. America A, Optics, Image Sci., Vis. A 11 (1994) 10.
[23] F. Martelli, A. Pifferi, D. Contini, L. Spinelli, A. Torricelli, H. Wabnitz, R. Macdonald, A. Sassaroli, G. Zaccanti, Phantoms for diffuse optical imaging based on totally absorbing objects, part 1: basic concepts, J. Biomed. Opt. 18 (2013) 6.
[24] L. Spinelli, et al., Determination of reference values for optical properties of liquid phantoms based on Intralipid and India ink, Biomed. Opt. Express 5 (2014) 7.
[25] Fabrizio Martelli, Samuele Del Bianco, Andrea Ismaelli, Giovanni Zaccanti, in Light Propagation through Biological Tissue and Other Diffusive Media: Theory, Solutions, and Software 2009 (SPIE Press, Bellingham, Washington).
[26] R. Cubeddu, C. D'Andrea, A. Pifferi, P. Taroni, A. Torricelli, G. Valentini, C. Dover, D. Johnson, M. Ruiz-Altisent, C. Valero, Nondestructive quantification of chemical and physical properties of fruits by time-resolved reflectance spectroscopy in the wavelength range 650–1000 nm, Appl. Optics 40 (2001) 538.

[27] V. Usenik, Franci Štampar, and Robert Veberič, Anthocyanins and fruit colour in plums (Prunus domestica L.) during ripening, Food Chem. 114 (2009) 2.
[28] J.R. Mourant, T. Fuselier, J. Boyer, T.M. Johnson, I.J. Bigio, Predictions and measurements of scattering and absorption over broad wavelength ranges in tissue phantoms, Appl. Optics 36 (1997) 4.
[29] P. Lanka, et al., Multi-laboratory performance assessment of diffuse optics instruments: the BITMAP exercise, J. Biomed Opt. 27 (2022) 7.